ACS APPLIED MATERIALS & INTERFACES

Research Article

www.acsami.org

# Thermal Conductivity of Ultrahigh Molecular Weight Polyethylene Crystal: Defect Effect Uncovered by 0 K Limit Phonon Diffusion

Jing Liu,[†] Zaoli Xu,[†] Zhe Cheng,[†] Shen Xu,[†] and Xinwei Wang*[,‡,†]

[†]Department of Mechanical Engineering, Iowa State University, 2010 Black Engineering Building, Ames, Iowa 50011, United States

[‡]School of Environmental and Municipal Engineering, Qingdao Technological University, Qingdao, Shandong 266033, People's Republic of China

**ABSTRACT:** Crystalline ultrahigh molecular weight polyethylene (UHMWPE) has the highest reported thermal conductivity at room temperature: 104 W/(m·K), while theoretical predictions proposed an even higher value of 300 W/(m·K). Defects and amorphous fraction in practical UHMWPE fibers significantly reduces the thermal conductivity from the ideal value. Although the amorphous effect can be readily analyzed based on the effective medium theory, the defect effects are poorly understood. This work reports on the temperature-dependent behavior (down to 22 K) of thermal diffusivity and conductivity of UHMWPE fibers in anticipation of observing the reduction in phonon density and scattering rate against temperature and of freezing out high-momentum phonons to clearly observe the defect effects. By studying the temperature-dependent behavior of thermal reffusivity (Θ, inverse of thermal diffusivity) of UHMWPE fibers, we are able to quantify the defect effects on thermal conductivity. After taking out the amorphous region's effect, the residual thermal reffusivities ($\Theta_0$) for the studied two samples at the 0 K limit are determined as $3.45 \times 10^4$ and $2.95 \times 10^4$ s/m$^2$, respectively. For rare-/no-defects crystalline materials, $\Theta_0$ should be close to zero at the 0 K limit. The defect-induced low-momentum phonon mean free paths are determined as 8.06 and 9.42 nm for the two samples. They are smaller than the crystallite size in the (002) direction (19.7 nm) determined by X-ray diffraction. This strongly demonstrates the diffuse phonon scattering at the grain boundaries. The grain boundary thermal conductance ($G$) can be evaluated as $G \approx \beta \rho c_p v$ with sound accuracy. At room temperature, $G$ is around 3.73 GW/(m$^2$·K) for S2, comparable to that of interfaces with tight atomic bonding.

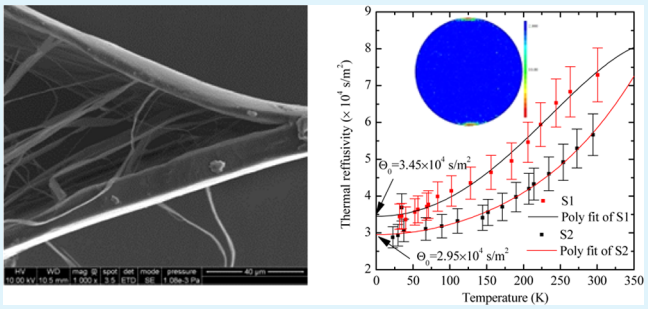


**KEYWORDS:** *polyethylene, thermal reffusivity, phonon scattering, heat capacity, interface thermal conductance*

## 1. INTRODUCTION

Typical polymers are well-documented to have a low thermal conductivity ($k$) in the order of 0.1 W/(m·K).[1] Polymers with a high $k$ have been promising candidates for industrial applications combining with their other characteristics such as mechanical flexibility, high corrosion resistance, lighter weight, and chemical stability.[2−4] Examples of applications include solar hot-water collectors, heat exchangers, electronic packaging,[5] membranes, microelectronic devices and nanocomposites,[6−8] gas sensors, field-effect transistors, and other fields.[9] Even though bulk polymers have a low $k$, the polymers can be manipulated and improved via structure engineering and tailoring to achieve relatively high $k$. Significant improvement is achieved in enhancing $k$ by introducing particles with a higher thermal conductivity such as ceramics,[10] metals,[11] graphene,[12,13] or carbon nanotube (CNT)[14] into the polymer matrix. Vasileiou et al. evaluated the $k$ of linear low-density polyethylene/thermally reduced graphene oxide (LLDPE/TRGO) composites. The $k$ of the composites is reported to be twice as large as that of pure LLDPE.[13] $k$ of single-walled CNT (SWNT)/high-density PE (HDPE) composites at room temperature increases from 0.5 to ∼3.5 W/(m·K) when SWNT loading is increased from 0 to 20 wt %.[15]

Until now, a lot of effort has been devoted to studying the factors which affect the $k$ of PE and how to improve its $k$. The $k$ of PE is dependent on many factors: temperature, the crystallinity of the PE fibers, the crystallite orientation, and the chain length.[1,16−21] Overall, at lower temperatures, the $k$ of semicrystalline PE fibers increases as temperature increases. When temperature is relatively high, $k$ increases with increasing temperature at a slower rate. Some experiments find that $k$ decreases after it reaches a maximum value at a certain temperature. This phenomenon that $k$ of PE has a peak value as temperature changes from 0 K to room temperature depends on the crystallinity of the PE fibers.[1] Scott et al. measured the $k$ of PE within the temperature range of 0.15−4 K. The $k$ of semicrystalline PE shows a $T^3$ dependence between 1 and 4 K while it shows a lower power temperature dependence when temperature is below 1 K.[19] Dyneema fiber, one kind of PE

Received: September 13, 2015
Accepted: November 21, 2015
Published: November 21, 2015





DOI: 10.1021/acsami.5b08578
ACS Appl. Mater. Interfaces 2015, 7, 27279−27288

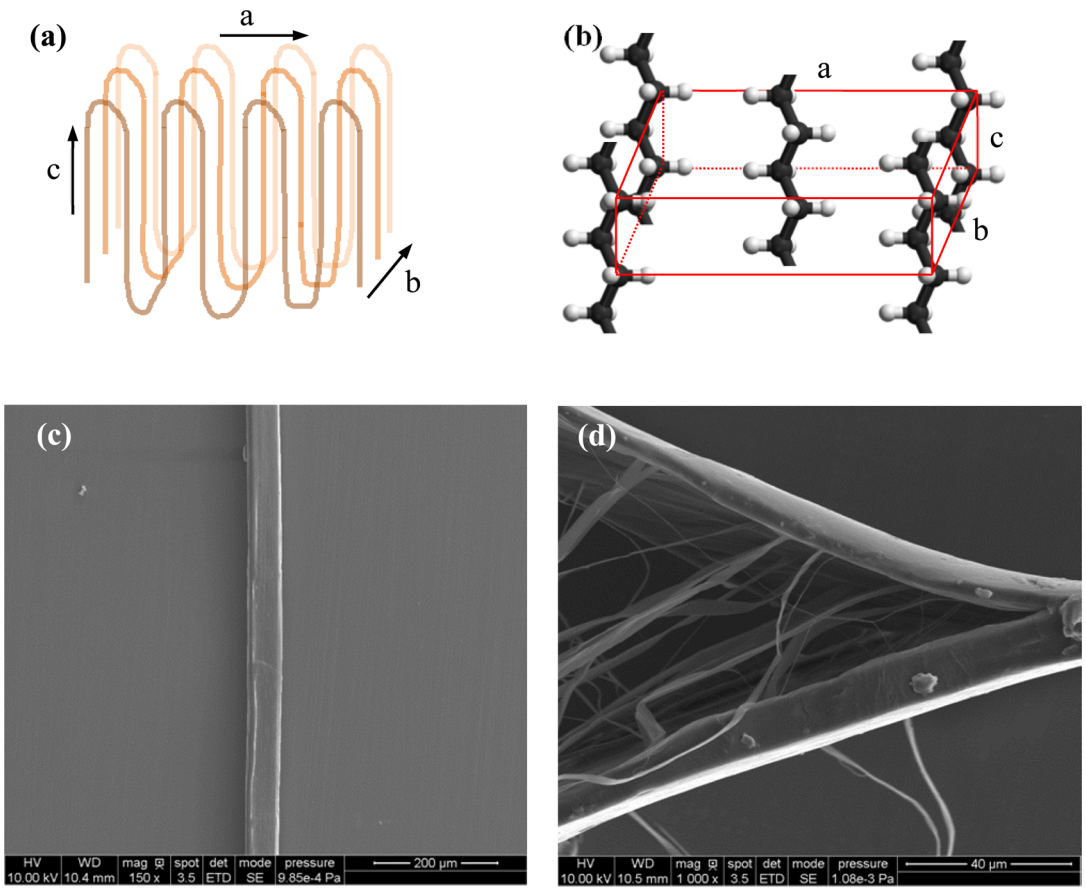


**Figure 1.** (a) Schematic molecular arrangement in crystalline PE fibers. The chains are carbon chains. The carbon chains shown in different colors are located on different lamellae. *c*-direction is always along the carbon chain direction. $a$ = 7.41 Å, $b$ = 4.94 Å, and $c$ = 2.55 Å. (b) Experimentally reported crystal structure of PE. (c) Scanning electron microscope (SEM) image of the sample before it is split into several fine fibers. (d) Sample that is broken into fine fibers mechanically to illustrate its internal stranded structure. The diameter of the sample used in this experiment is ∼50 $\mu$m. The finest split fiber could be ∼1 $\mu$m thick. This concludes that the large fiber is composed of fine fibers aligned along the axial direction.

fiber with sound crystalline structure, low defect density, and high crystal alignment, has a $k$ of about 30 W/(m·K) at room temperature.[18] The order of $k$ of amorphous PE chain increases from ∼0.001 to ∼0.1 W/(m·K) as the chain length increases.[20] $k$ of stretched PE fibers is found to increase from 0.55 to 14 W/(m·K) due to stretching. This is mainly due to the fact that the alignment of crystallite in PE fiber is enhanced by stretching.[17,22] For single PE chains, the length of the chain plays an important role in determining the thermal conductivity; molecular dynamics (MD) simulations shows that $k$ of a single PE chain can be ∼300 W/(m·K) when the chain is longer than 40 nm.[23] Shen et al. found that the $k$ of ultradrawn nano PE fiber with a length and diameter of 290 $\mu$m and 130 nm could be as high as 104 W/(m·K). The authors attribute the high $k$ to extended chains and crystallite orientation after the fiber had been drawn.[5]

Figure 1a shows a schematic molecular arrangement in crystalline regions in semicrystalline PE fibers. Figure 1b shows the experimentally reported crystal structure of PE.[24] It can be seen that each PE chain has an extended planar zigzag conformation. The PE chains with different colors shown in Figure 1a are on different lamellae. Since the interchain van der Waals force is much weaker than the intrachain covalent force, $k$ of PE along the chain direction (*c*-direction in Figure 1a,b) is much larger than those along the other two directions.[17] Further investigation of the molecular structure of our samples shows that the *c*-direction is highly aligned along the fiber axis direction along which the $k$ was measured. More details about the crystallite orientation will be given when the molecular structure of the samples is discussed.

In this work, first we measure the thermal diffusivity ($\alpha$) and $k$ of semicrystalline ultrahigh molecular weight polyethylene (UHMWPE) fibers from room temperature down to 22 K using the transient electrothermal (TET) technique.[25] After subtracting the effect of the amorphous region, the inverse of thermal diffusivity of PE fibers, termed as thermal reffusivity in this work ($\Theta$), is studied for its variation from around room temperature down to 22 K. This allows us to identify the effect of defect−phonon scattering and assess the mean free path due to defect-induced phonon scattering in crystalline regions ($l_0$). And then we evaluate the volumetric heat capacity ($\rho c_p$) and the interface thermal conductance ($G$) of fully crystalline macro PE fibers with a new method that includes both experimental and theoretical studies.

## 2. SAMPLE STRUCTURE CHARACTERIZATION

Commercial UHMWPE fibers with high strength and extended chains from Minifibers Company are used in this experiment. Their modulus is around 850 g/den (den = denier), and the density is 0.96 g/cm$^3$. The molecular mass is usually between 2 and 6 million Da for UHMWPE. The molecular structure of the fiber is characterized using a confocal Raman system (Voyage, B&W Tek, Inc. and Olympus BX51). A 532 nm Raman laser of 16 mW is focused on the fiber with a


DOI: 10.1021/acsami.5b08578
ACS Appl. Mater. Interfaces 2015, 7, 27279−27288

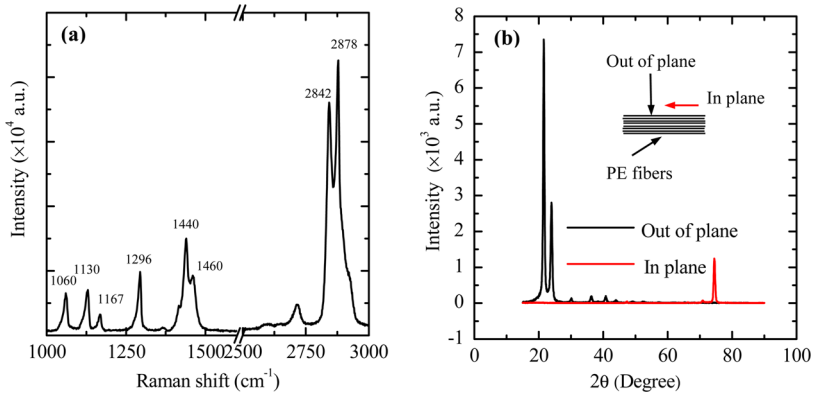


**Figure 2.** (a) Raman spectrum of our studied UHMWPE. (b) X-ray diffraction patterns for the UHMWPE fibers. The inset in panel b shows the schematic experimental setup for determining the crystallite size in the (002) direction. The normal lines of the X-ray beam are out of the plane of PE fibers and in the plane of PE fibers, respectively.

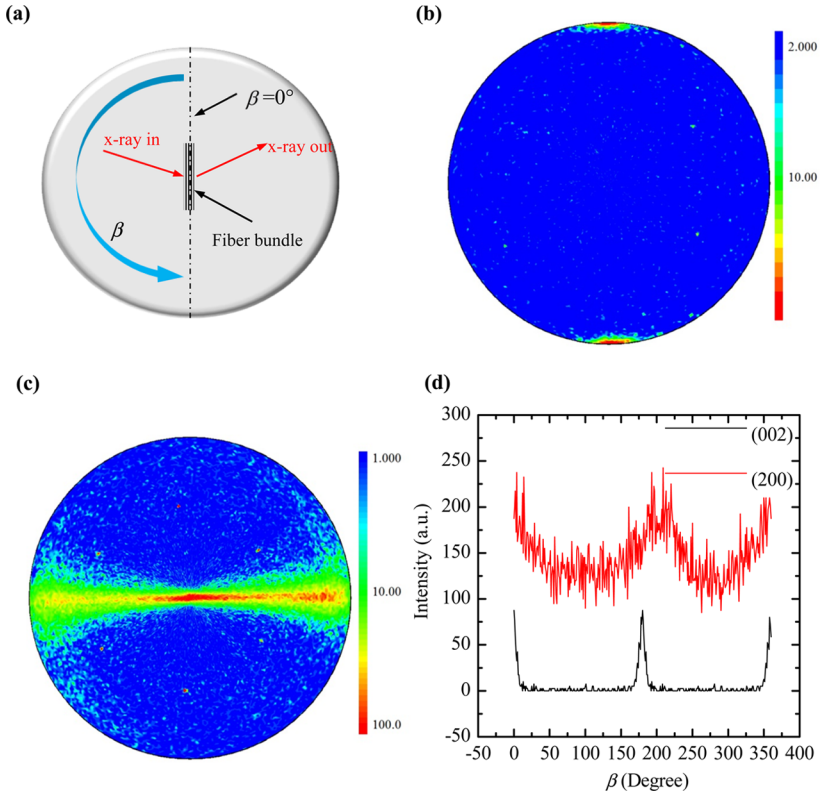


**Figure 3.** (a) Schematic of the XRD experiment with $\beta = 0°$. (b) Pole figure for (002) plane. (c) Pole figure for (200) plane. (d) Intensity variation along a varying $\beta$ with a fixed $\alpha$ corresponding to a twisting motion. (002) plane: $\alpha = 0°$. (200) plane: $\alpha = 90°$.

50× lens. A 20 s integration time is used to obtain a representative spectrum of the fibers as shown in Figure 2a. Sharp peaks are observed at 1060 and 1130 $cm^{-1}$ for C−C stretching mode and peaks at 1167 and 1296 $cm^{-1}$ for $CH_2$ twisting mode for all-trans -$(CH_2)_n$- in the crystalline structures. The existence of amorphous structures is illustrated by the amorphous peaks at 1440 and 1460 $cm^{-1}$. The 2842 and 2878 $cm^{-1}$ peaks indicate $CH_2$ stretching modes in the fiber which are not related to the crystalline structures.[26,27] When we place a PE fiber on a glass slide, and use another glass slide to press the fiber, we find the PE fiber can be mechanically split into finer ones. Figure 1c shows the scanning electron microscope (SEM) image of the sample before it is split into several finer fibers. It can be seen that the cross-section of the fiber is not exactly round. Figure 1d shows that a sample is split into several fine fibers mechanically, which illustrates its internal stranded structure. The diameter of the sample used in this experiment is ∼50 $\mu$m. The finest split fiber could be ∼1 $\mu$m thick. This concludes that the large fiber is composed of fine fibers aligned along the axial direction.

Figure 2b gives the X-ray diffraction (XRD, Rigaku Smartlab diffractometer) patterns for the UHMWPE fibers. It can be seen that the sample is highly crystalline and the crystallinity is determined to be 91.9%. The crystallite size in the (002) direction is determined to be around 19.7 nm. For the out-of-plane directions, the crystallite size is 12 ± 1.6 nm. The inset in Figure 2b shows the schematic experiment setup for determining the crystallite size in the (002) direction. The normal lines of the X-ray beam are perpendicular and parallel to the plane of PE fibers, respectively. Detailed crystalline structure orientation is analyzed based on the XRD pole figures. Figure 3a shows the schematic of the XRD experiment with $\beta = 0°$. The pole figures for the (002) plane and the (200) plane are shown in Figure 3b,c. Figure 3d shows the intensity variation along a varying $\beta$ with a fixed $\alpha$ corresponding to a twisting motion: for (002) plane, $\alpha = 0°$;


DOI: 10.1021/acsami.5b08578
ACS Appl. Mater. Interfaces 2015, 7, 27279−27288

for (200) plane, $\alpha = 90°$. Combining b–d, we could conclude that the crystallite orientation (the *c*-direction in Figure 1b) is highly along the axial direction of the fiber. For the (002) plane, the orientation distribution shown in Figure 3d has a very small angle distribution along the fiber axis: 8.28° for full width at half-maximum. Figure 3b and the intensity distribution in Figure 3d show the (200) plane is more spread out (all along $\alpha$ of 0–90°) than the (002) plane. The excellent orientation of the PE crystal in the fiber also explains why they have a high *c*-direction thermal conductivity (~25 W/(m·K) at room temperature), which is larger than that of many unprocessed PE fibers.

## 3. THERMAL CONDUCTIVITY OF UHMWPE

**3.1. Thermal Characterization Principle.** Since there are differences among UHMWPE fibers even though they are produced at the same time, two UHMWPE fibers are used to do the experiment (S1 and S2). Geometric parameters and surface morphology of S2 obtained under SEM are shown in Figure 4a. Since we could not make multiple samples with the exactly same diameter and length, the samples' length and diameter are 1.32 mm and 49.08 $\mu$m for S1 and 1.17 mm and 45.17 $\mu$m for S2. The thermal diffusivity and conductivity of the two UHMWPE fibers are measured from 290 K down to 10 K by using the TET technique.[25,28] First, the UHMWPE fiber is coated with 15 nm thickness iridium in order to make it electrically conductive. This is needed to make it applicable for TET measurement. The sputtering machine is Quorum Q150T S.

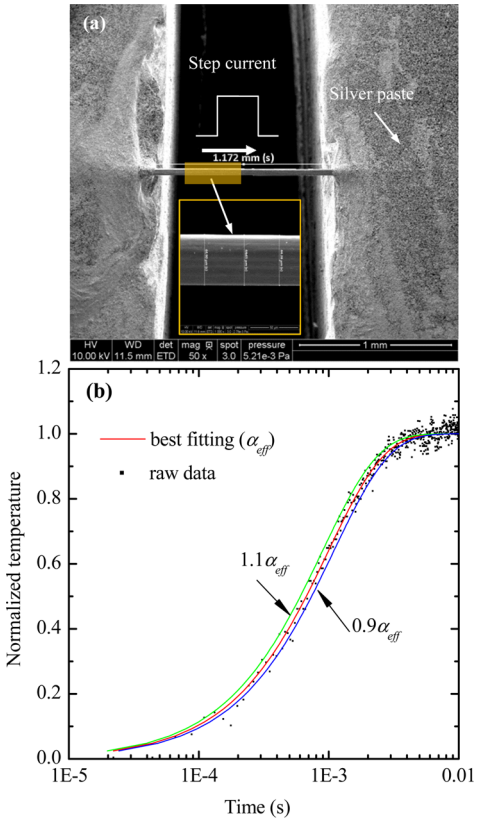


**Figure 4.** (a) SEM image of an UHMWPE fiber connected between two electrodes during TET measurement. (b) Normalized temperature variation and TET fitting result when a 2.2 mA square current with a 5 Hz modulation frequency is applied to S2 at 10 K (where, for example, 1E-5 represents $1 \times 10^{-5}$). The accuracy of the fitting is demonstrated by comparing two theoretical curves with 10% variation of the best fitted thermal diffusivity. The effective thermal diffusivity ($\alpha_{eff}$) that includes the effect of radiation and iridium is determined as $3.02 \times 10^{-5}$ m$^2$/s.

As shown in Figure 4a, the to-be-measured sample is suspended between two aluminum electrodes and placed in a vacuum chamber of a cryogenic system (CCS-450, JANIS). The fiber–electrode contact is secured with silver paste to ensure excellent electrical and thermal contact. The vacuum level remains under 0.5 mTorr by a liquid nitrogen cold-trapped mechanical vacuum pump to eliminate the effect of heat convection in the measurement. During the thermal characterization, a square current offered by a current source (Keithley 6221) is fed through the fiber to induce Joule heating. The temperature rise caused by the Joule heating will lead to a rise of the sample resistance and thus the voltage over the fiber. An oscilloscope (Tektronix DPO3052) is used to monitor the voltage evolution over the fiber. The normalized temperature evolution is derived from the voltage evolution. Once the normalized temperature evolution is obtained, the thermal diffusivity of the sample can be obtained by fitting the normalized temperature change curve against time. The TET technique has been evaluated rigorously and used successfully in our laboratory to measure various conductive and non-conductive micro-/nanoscale fibers. The measurement accuracy has been fully evaluated by measuring reference materials and comparing the results with reference values. More details could be found in the references.[25,29,30]

Figure 4a shows the schematic setup and experimental principle of the TET technique. Since the aluminum electrodes used in this experiment are much larger than the sample dimension, the temperature of the electrodes can be assumed unchanged even though a small current is through it. The boundary conditions can be described as $\Delta T(x{=}0) = 0$, where $\Delta T = T - T_0$ ($T_0$, room temperature). The heat conduction along the sample can be treated as one-dimensional due to the sample's very high aspect ratio (length to diameter). The governing equation is

$$\frac{\partial(\rho c_p T)}{\partial t} = k\frac{\partial^2 T}{\partial x^2} + \dot{q} \tag{1}$$

where $\rho$, $c_p$, and $k$ are the density, specific heat, and thermal conductivity of the sample, respectively, $\dot{q}$ is the electrical heating power per unit volume. It has the form of $I^2R_s/AL$, where $A$ and $L$ are the cross-sectional area and length of the sample, respectively. The normalized temperature rise, which is defined as $T^*(t) = [T(t) - T_0]/[T(t\to\infty) - T_0]$, is solved as[25]

$$T^* = \frac{96}{\pi^4}\sum_{m=1}^{\infty}\frac{1 - \exp[-(2m-1)^2\pi^2\alpha_{eff}t/L^2]}{(2m-1)^4} \tag{2}$$

where $\alpha_{eff}$ is the sample's effective thermal diffusivity that includes the effect of radiation and iridium coating. After the voltage evolution is obtained, the experimental normalized temperature increase can be calculated as $(V - V_0)/(V_1 - V_0)$, where $V_0$ and $V_1$ are the initial and final voltages over the sample.

The theoretical normalized temperature rise is calculated according to eq 2 by using different trial values of $\alpha_{eff}$ and is compared with the experimental results. The trial value which gives the best fit of the experiment data is taken as the sample's effective thermal diffusivity ($\alpha_{eff}$). The real thermal diffusivity ($\alpha_{real}$) of the sample is obtained after subtracting the effect of radiation and iridium as[31,32]


DOI: 10.1021/acsami.5b08578
ACS Appl. Mater. Interfaces 2015, 7, 27279–27288

$$\alpha_{real} = \alpha_{eff} - \frac{16\varepsilon\sigma T^3 L^2}{\pi^2 D\rho c_p} - \frac{L_{Lorenz} TL}{RA\rho c_p} \quad (3)$$

$\varepsilon$ and $\sigma$ are emissivity and the Stefan−Boltzmann constant, respectively. $L_{Lorenz}$ is the Lorenz number ($2.45 \times 10^{-8}$ WΩ/K$^2$) for iridium. Figure 4b shows the experimental data of the $V - t$ curve and fitting result when the experiment is conducted at 10 K ambient temperature with a square current of 2.2 mA fed to S2. The corresponding normalized voltage increase is 1.05%. The modulation frequency of the square-wave current is 5 Hz, and the corresponding period is much longer than the time taken for the sample to reach the steady state. The rise time of the current source is 2 $\mu$s, much shorter than the time for the sample to reach the steady state. Excellent fitting is obtained in the results. The accuracy of the fitting is demonstrated by comparing two fitting curves with 10% variation of the effective thermal diffusivity which is shown in Figure 4b. We find that the fitting curve is sensitive to the selected effective thermal diffusivity, which indicates that the obtained effective thermal diffusivity has a high accuracy. The effective thermal diffusivity is determined to be $3.02 \times 10^{-5}$ m$^2$/s for S2 at 10 K.

**3.2. Thermal Diffusivity and Thermal Conductivity Variation against Temperature.** The effective thermal diffusivity of S1 and S2 is characterized with the TET technique from room temperature down to 10 K. Based on the sample's crystallinity of 91.9% (obtained previously using XRD), the volumetric heat capacity of this sample is evaluated using the heat capacity of extrapolated crystalline and amorphous PE as a function of temperature given in Chang's work.[33] The densities of crystalline PE and amorphous PE are determined to be 1000 and 851.5 kg/m$^3$ according to previous work.[16] The volumetric heat capacity of the sample is derived from the literature according to the following equation: $(\rho c_p)_{sample} = (\rho c_p)_c \chi + (\rho c_p)_a (1 - \chi)$, in which $\chi$ is crystallinity and it is determined by XRD analysis. The subscripts "c" and "a" are for crystal and amorphous structure. Figure 5a shows the determined $\rho c_p$ variation against temperature for the sample. This result is used in eq 3 to subtract the effect of radiation and iridium coating. Here we use an emissivity of 0.2 to subtract the effect of radiation on thermal diffusivity. The emissivities of PE and iridium are ∼0.1 and 0.3, respectively. The upper half-surface of the PE fiber is coated with iridium while the lower is not, so we use 0.2 as the effective emissivity.

Figure 5b shows the temperature dependence of $\alpha_{real}$ for S1 and S2. The uncertainties of the real thermal diffusivity measurements are presented by error bars. The temperature of the sample increases a little bit due to Joule heating, so corrections are made to represent the real temperature of the sample for the measured thermal diffusivity. The $R-T$ relationship of the sample is first obtained, and then the average of the initial and the steady-state resistances in the TET measurement is used to calculate the characteristic temperature of the sample for reporting its thermal properties. This is why the lowest temperature is a little bit higher than 10 K in Figure 5b. During the TET test, the temperature rise is commonly less than 10 K when the voltage is increased by 3% or less. From Figure 5b, it can be seen that $\alpha_{real}$ decreases with increased temperature. This changing trend is almost linear. For S2, the thermal diffusivity decreases from $3.011 \times 10^{-5}$ to $2.722 \times 10^{-5}$ m$^2$/s (by 9.6%) when temperature increases from 22 to 110 K. The thermal diffusivities of S2 at the lowest temperature and 294 K are determined to be $3.011 \times 10^{-5}$ and $1.550 \times 10^{-5}$ m$^2$/s, respectively. The increasing thermal diffusivity with decreased

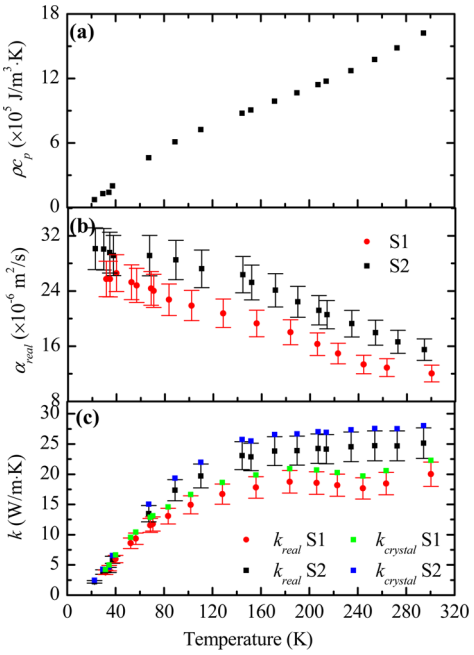


**Figure 5.** (a) Volumetric heat capacity against temperature. (b) Variation of real thermal diffusivity with temperature for S1 and S2. (c) Variation of real thermal conductivity with temperature for S1 and S2. The thermal conductivity for pure crystalline regions in S1 and S2 is also given after subtracting the amorphous effect and shown in the figure. The uncertainties of the measurements are presented with error bars for S1 and S2.

temperature points out that heat transfers faster in the fiber at lower temperatures. It is understood that the thermal diffusivity is a combined effect of both thermal conductivity and specific heat. Its variation against temperature is more related to the change of the phonon mean free path in the material. More discussions are given later for using the inverse of thermal diffusivity of crystalline regions in S1 and S2 (thermal reffusivity) to study the defect−phonon scattering effect.

The thermal conductivity ($k_{real}$) of the sample is obtained according to the equation: $k_{real} = \alpha_{real}(\rho c_p)_{sample}$. Figure 5c shows the variation of $k_{real}$ against temperature for S1 and S2. $k_{real}$ of S1 and S2 are determined to be 20 and 25.1 W/(m·K) at room temperature, respectively. They are much smaller than that of the nano PE fiber measured by Shen et al.[5] In their work, $k$ was found to be as high as ∼104 W/(m·K). This difference may arise partly from the amorphous effect. Samples in our experiment are micro PE fibers with amorphous structure effect, while the nanofiber used in their experiment is stretched to improve the fiber toward to an "ideal" single crystalline fiber. Here, we give an estimate to rule out the amorphous effect and defects-induced phonon scattering effect. The semicrystalline UHMWPE fiber used in the experiment can be considered as a two-phase system composed of crystallite and amorphous regions. The amorphous phase can be regarded as being distributed uniformly among the rich crystalline regions. In our work, the crystallinity is very high, 91.9%, so the amorphous region only takes a small volume fraction of 8.1%. Under such conditions, according to Maxwell effective medium theory, the relationship of the effective thermal conductivity of a mixture ($k_e$) and the thermal conductivity of the crystallite ($k_{crystal}$) is $(k_e/k_{crystal}) = 1 + 3(\gamma - 1)(1 - \chi)/[(\gamma + 2)(\gamma - 1)(1 - \chi)]$.[34] Here $\gamma$ is the ratio of thermal conductivity of amorphous to thermal conductivity of


DOI: 10.1021/acsami.5b08578
ACS Appl. Mater. Interfaces 2015, 7, 27279−27288

crystallite, and $\chi$ is crystallinity. Since the thermal conductivity of the amorphous region is negligible compared with that of crystalline UHMWPE, we have $(k_e/k_{crystal}) = 1 - 3(1-\chi)/(1+\chi)$ as very precise evaluation. After taking out the amorphous effect, the thermal conductivity will be 11.5% higher. The predicted $k_{crystal}$ for S1 and S2 are also shown in Figure 5c. In Choy's work, the orientation effect is also considered when measuring the thermal conductivity of PE samples. The orientation effect is depicted by an orientation function $f_c$: $f_c = [3\langle\cos^2\theta\rangle - 1]/2$, among which $\theta$ is the angle between the *c*-direction [shown in Figure 1a] and the fiber drawn direction. The thermal conductivity parallel to the drawing direction ($k_{\parallel}$), thermal conductivity perpendicular to chains ($k_{c\perp}$) direction and the thermal conductivity of amorphous region ($k_a$) has the following relationship: $((k_{\parallel} - k_a)/(k_{\parallel} + 2k_a)) = \chi[(k_{c\perp}/k_a) - 1 + 3\langle\cos^2\theta\rangle]/(k_{c\perp}/(k_a + 2))$.[1,17] However, the orientation effect is not taken into consideration in this work because the chain directions in the measured samples are highly along the fiber direction, which is detailed in Figure 3.

The predicted $k_{crystal}$ is still much smaller than that (104 W/(m·K)) obtained by Shen et al. In our work, we found that the sample can be easily split to finer fibers after mechanical twisting. Panels c and d of Figure 1 show the SEM images of the sample before and after being split. This concludes that the large fiber indeed is composed of fine fibers aligned along the axial direction. We feel the grain boundary resistance, crystallite size, and alignment could contribute to the difference a lot. Since the PE crystal of our sample is highly aligned, so the grain boundary resistance and crystallite size have more contributions to this difference. The large thermal conductivity obtained by Shen et al. is for ultradrawn nanofibers, so the crystallite size (grain size) could be a big-role player.

From Figure 5c, it is found that $k_{real}$ increases with increased temperature with a relatively faster rate at lower temperatures and kind of saturates when temperature is above 150 K. $k_{crystal}$ shows the same trend as $k_{real}$. Phonon scattering dominates the thermal transport in both crystalline and amorphous regions.[35] The crystalline region largely determines the $k$ of the fibers measured in this work; the following quantitative discussion about the samples is focused on the phonon scattering in crystalline regions. For any specific phonon with a particular wave vector $\boldsymbol{\kappa}$ and angular frequency $\omega$, single relaxation time approximation is valid. Under one relaxation time approximation, it is well-known that $k = Cvl$ for 1-D molecular structures. $C$ is the volumetric heat capacity, $v$ is the phonon velocity, and $l$ is the mean free path. $v$ varies little with temperature, so the trend of $k$ is more determined by $C$ and $l$ jointly. Defects-induced phonon scattering and phonon to phonon scattering (Umklapp scattering) make up the phonon scattering jointly. So we could have

$$l^{-1} = l_0^{-1} + l_i^{-1} \quad (4)$$

according to Matthiessen's rule,[36] where $l_0$ and $l_i$ are defects-induced mean free path and mean free path due to phonon−phonon scattering, respectively. This single relaxation approximation is used to qualitatively explain the observed thermal conductivity variation trend against temperature. $l_i$ decreases as temperature increases while $C$ increases with increased temperature.[33,37] In section 3.3, detailed discussion is given about the physics on why $l_i$ decreases as temperature increases. Due to the existence of $l_0$, $l$ decreases with a lower rate compared with that of $l_i$ as temperature increases. This causes $k_{crystal}$ to decrease with decreased temperature and saturate at higher temperatures. The phenomenon that $k_{crystal}$ reaches a peak value around 100 K for other PE fibers is not observed in our samples.[1] It is because, in our samples, the size of defects is comparable with the mean free path due to phonon−phonon scattering. More discussions are provided in the following sections. It is more convenient to look at the inverse of thermal diffusivity of crystalline regions (thermal reffusivity) for studying the thermal transport process.

**3.3. Defect Effect on Thermal Conductivity Uncovered by 0 K Limit Phonon Diffusion.** First of all, we plot the variation of thermal reffusivity of crystalline regions ($\alpha^{-1}$) against temperature. The results are shown in Figure 6. Here

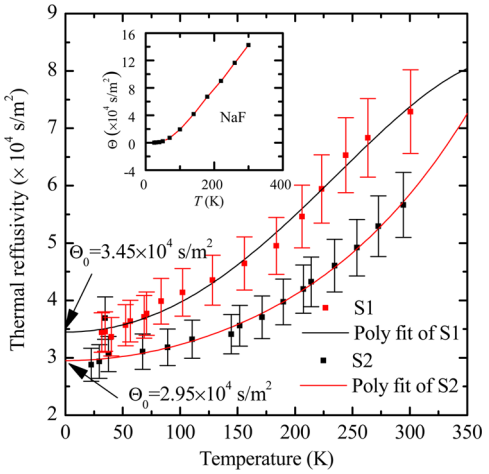


**Figure 6.** Variation of the thermal reffusivity of crystalline regions with temperature for S1 and S2. The uncertainties of the measurements are presented with error bars. The residual thermal reffusivities for S1 and S2 are determined as 3.45 × $10^4$ and 2.95 × $10^4$ s/m$^2$, respectively. This is caused by the existence of defects in the UHMWPE fibers. The inset shows the variation of thermal reffusivity with temperature for crystalline sodium fluoride for comparison purpose. Its residual thermal diffusivity is close to zero since the defects in it are rare.

the thermal reffusivity (denoted as Θ) was first defined and used by Xu et al. to characterize the phonon thermal resistivity.[38] Θ plays the same role as electrical resistivity in reflecting the phonon scattering and defect scattering of energy/charge carriers. For electron charge transport, phonon−electron scattering and defect−electron scattering determine the electrical resistivity jointly: $\rho = (m/ne^2\tau) = \rho_L + \rho_0$ ($\rho_L$, the resistivity by thermal phonons; $\rho_0$, the resistivity from the static defects−phonon scattering). At the 0 K limit, a finite residual electrical resistivity $\rho_0$ demonstrates the existing defect in metals. If there are very rare defects, $\rho_0$ approaches zero at the 0 K limit. Although the electrical resistivity is the inverse of electrical conductivity, the reciprocal of thermal conductivity $k$ cannot be used similarly to define a thermal resistivity to describe the phonon scattering since $\rho c_p$ is involved in $k$ and it also changes with temperature. Θ is defined to characterize the phonon scattering for the thermal transport behavior after ruling out the effect of $\rho c_p$. Θ is solely determined by the phonon scattering inside the material and is expressed as the following equation in terms of phonon velocity ($v$) and mean free path ($l$): $\Theta = 3v^{-1}l^{-1}$. $l$ is inversely proportional to phonon scattering intensity. Therefore, Θ directly reflects the phonon scattering behavior. As will be discussed later, Θ also consists of two parts: one is induced by phonon−phonon scattering, and the other part is static phonon scattering by defects. Just like


DOI: 10.1021/acsami.5b08578
ACS Appl. Mater. Interfaces 2015, 7, 27279−27288

electrical resistivity, the variation of Θ versus temperature can be used to identify the residual value at the 0 K limit to evaluate the defects in the material.

Thermal reffusivity can be used to characterize different phonon scattering mechanisms. The way Θ changes with temperature ($\partial\Theta/\partial T$), and its residual value at the 0 K limit all can be used to provide unprecedented details of phonon scattering. For any specific $\omega$ and $\kappa$, we already have $l^{-1} = l_0^{-1} + l_i^{-1}$. The occupancy of a phonon mode at a specific temperature $T$ is described by the Bose−Einstein distribution,[39]

$$\langle n \rangle = \frac{1}{e^{\hbar\omega/k_B T} - 1} \tag{5}$$

where $\hbar$ is Planck's constant and $k_B$ the Boltzmann constant. $\langle n \rangle$ becomes very small when temperature goes to the 0 K limit, indicating the phonon−phonon scattering is scarce and $l_i \to \infty$. The phonon−phonon scattering vanishes as temperature goes down to 0 K, and the defect-induced scattering becomes the only phonon scattering effect at the 0 K limit. For any specific $\omega$ and $\kappa$, $k = Cvl$ for the 1-D molecular structure in PE. Combining with eq 4, we get $\Theta = l^{-1}v^{-1} = v^{-1}(l_0^{-1}+l_i^{-1}) = (\Theta_0+\Theta_i)$. As temperature goes down to 0 K, $\Theta_i$ goes to zero; the thermal reffusivity is left with $\Theta_0$ at 0 K. For all phonons, the accumulated effect of their residual thermal reffusivity gives the one measured in our experiment. Defects-induced phonon scattering plays a major role in limiting $k$. If there are no defects in the material, Θ should approach zero when temperature is zero. From Figure 6, it can be seen that Θ approaches a nonzero value as temperature goes down to 0 K. The residual thermal reffusivity $\Theta_0$ of the two samples are indicated in Figure 6: $3.45 \times 10^4$ s/m$^2$ for S1 and $2.95 \times 10^4$ s/m$^2$ for S2. The trend of $\Theta \sim T$ curve is very similar to the change of electrical resistivity change with temperature for metals: if the defects in the material have substantial effect on scattering, when temperature goes to 0 K, Θ and $\rho$ do not approach zero; rather they have finite residual values. Many crystalline materials have been used in our laboratory to examine the thermal reffusivity theory. Θ of silicon, germanium, sodium chloride, and sodium fluoride are found to show different behaviors from the UHMWPE fibers. For a material with negligible defects effect, $\Theta_0$ becomes very small (negligible) at the 0 K limit. The $\Theta - T$ relationship for sodium fluoride (NaF) crystal shown in the inset in Figure 6 strongly proves this point: Θ becomes almost zero at the 0 K limit.[40,41]

After knowing $\Theta_0$, we could derive the defects-induced phonon scattering mean free path ($l_0$) in crystalline regions for the two samples. As $T \to 0$ K, phonons with different frequencies can be reasonably considered to share the same $l_0$ since only a few acoustic phonons with low frequencies are excited according to eq 5. Thus, we get

$$\Theta_0 = \frac{\rho c_p}{k}\bigg|_{T\to 0} = \frac{\rho c_p}{\rho c_p v l_0}\bigg|_{T\to 0} = \frac{\sum_{M=1}^{18}\int_0^{\omega_D}\frac{\partial U_M}{\partial T}\,d\omega}{\sum_{M=1}^{18}\int_0^{\omega_D}\frac{\partial U_M}{\partial T} l_0 v_\omega\,d\omega}\bigg|_{T\to 0} \tag{6}$$

For the AIREBO model of the PE crystal,[42] there are 18 phonon branches: four acoustic phonon branches and 14 optical phonon branches. $M$ denotes the number of phonon branches. $U_M$ is the thermal energy for the $M$th phonon branch; $v_\omega$ is the phonon velocity, and it is dependent with the frequency $\omega$. In polymers, acoustic phonons dominate the scattering effect for thermal transport, so only acoustic phonons are taken into consideration when estimating phonon velocities. For optical phonons, the phonon velocity is almost zero, so we ignore it here. The phonon velocity is $v = (\partial\omega(\kappa)/\partial\kappa)$ as defined. The phonon velocity variations for four acoustic phonon branches against the normalized frequency are shown in Figure 7b. Number indices identify the two transverse (1 and 2) branches, longitudinal (3), and torsional acoustic polarizations (4). The phonon velocity will be used for evaluating the volumetric heat capacity and the defect-induced phonon mean free path evaluation, and will be discussed later. $\omega_D$ is the cutoff frequency for each phonon branch. For acoustic phonon branches, the thermal energy $U_M$ is given as

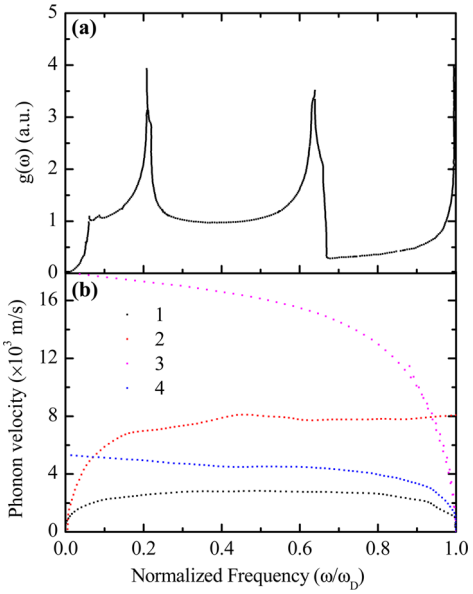


**Figure 7.** (a) Density of state for complete frequency distribution. (b) Phonon velocity for four acoustic phonon branches. The legends identify the two transverse (1 and 2) branches, longitudinal (3), and torsional acoustic polarizations (4).

$$U_M = \int g(\omega)\, n(\omega)\hbar\omega\, d\omega = \int_0^{\omega_D} g(\omega)\left(\frac{\hbar\omega}{e^{\hbar\omega/k_B T} - 1}\right) d\omega \tag{7}$$

among which $g(\omega)$ is the density of state and $g(\omega)$ is shown in Figure 7a.[43]

The volumetric heat capacity $C_a$ for the acoustic phonons becomes

$$C_a = \sum_{M=1}^{4}\int_0^{\omega_D} g(\omega) k_B \left(\frac{\hbar\omega}{k_B T}\right)^2 \frac{e^{\hbar\omega/k_B T}}{(e^{\hbar\omega/k_B T} - 1)^2}\, d\omega \tag{8}$$

For optical phonons, the thermal energy is given by the Einstein model: $U = N\langle n \rangle \hbar\omega$, among which $N$ is the number of primitive cells. Thus, we have

$$C_o = \sum_{M=1}^{14} N k_B \left(\frac{\hbar\omega}{k_B T}\right)^2 \frac{e^{\hbar\omega/k_B T}}{(e^{\hbar\omega/k_B T} - 1)^2} \tag{9}$$

The total volumetric heat capacity is the combination of two kinds of phonons. Figure 8a shows the curves of volumetric heat capacity against temperature obtained through reference and the calculation method depicted earlier. The data shown in red squares are the reference values; data in black squares and green squares indicate the volumetric heat capacities for 14


DOI: 10.1021/acsami.5b08578
ACS Appl. Mater. Interfaces 2015, 7, 27279−27288

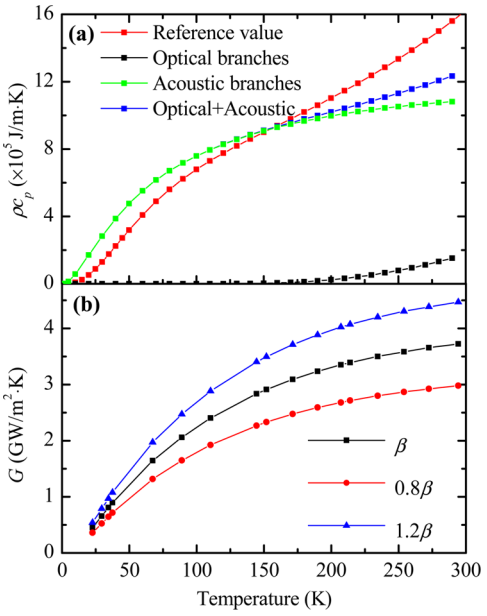


**Figure 8.** (a) Volumetric heat capacity against temperature. It shows contributions from different phonon modes. The data shown in red squares are the reference values; data in black squares and green squares indicate the volumetric heat capacity for 14 optical phonon branches and four acoustic phonon branches, respectively. Data shown in blue squares are the calculated volumetric heat capacity. (b) Interface thermal conductance varying with temperature for S2. The interface thermal conductance range is given when $\beta$ changes by ±20%.

optical phonon branches and four acoustic phonon branches, respectively. Data shown in blue squares are the calculated total volumetric heat capacities. The typical frequencies for the optical phonon branches are between 30 and 90 THz. From Figure 8a, it can be seen that a significant portion of the optical phonons contributes little to the total specific heat compared with that of acoustic phonons. Considering the fact that the optical phonons have almost zero velocity and significantly smaller specific heat, the optical phonons contribute much less to the thermal transport, so the optical phonons effect can be neglected when calculating the thermal conductivity. The calculated volumetric heat capacity is very close to the reference experimental value, which validates the theory to obtain the total volumetric heat capacity for PE crystals. The little difference is possibly induced by the following fact: our frequency of phonons is based on the results of PE single molecular chain, and the chain−chain interaction is not considered. This will omit some energy contribution to the overall specific heat. Combining eqs 7, 8, and 9, $\Theta_0$ is obtained as

$$\Theta_0 = \left. \frac{\sum_{M=1}^{4}\int_0^{\omega_{D_M}} g(\omega)k_B(\hbar\omega/k_BT)^2 e^{\hbar\omega/k_BT}/(e^{\hbar\omega/k_BT}-1)^2 d\omega + \sum_{M=5}^{18} Nk_B(\hbar\omega/k_BT)^2 e^{\hbar\omega/k_BT}/(e^{\hbar\omega/k_BT}-1)^2}{l_0\sum_{M=1}^{4}\int_0^{\omega_{D_M}} g(\omega)k_B(\hbar\omega/k_BT)^2 e^{\hbar\omega/k_BT}/(e^{\hbar\omega/k_BT}-1)^2 v_\omega d\omega} \right|_{T\to 0} \quad (10)$$

By knowing $\Theta_0$, $g(\omega)$, and $v_\omega$, $l_0$ can be determined. Based on eq 1 and $\Theta_0$. $l_0$ for S1 and S2 are determined to be 8.06 and 9.42 nm. $l_0$ of the two samples are both comparable, but smaller than the grain size ($l_g$ = 19.7 nm) determined by XRD. It indicates that the grain boundary phonon scattering is very strong, which makes the phonons almost lose all the original information after passing the grain interface. We can tell that the grain boundary scattering is totally diffuse; the boundary-induced phonon scattering mean free path should be shorter than the XRD determined grain size based on the mean free path physical meaning: after traveling displacement of $l_0$, the phonons are left with $e^{-1}$ times of the original energy. Here, $\Theta_0$ is evaluated to tell the difference in defects-induced phonon scattering mean free path of crystalline regions for the two samples. It is better to tell the defect difference between S1 and S2 directly through other methods to verify the results gained in our experiment. Due to the very small sample size (~50 $\mu$m diameter), our current XRD system could not give a sound signal for a single fiber to distinguish the defect difference between individual fibers. Also our Raman spectrum study could not tell the tiny defect difference between samples. To our best knowledge, there is no direct and quick technology to measure the defect-induced phonon scattering mean free path while the mean free path of phonons could be calculated from experimental data.[37,44] We believe that thermal reffusivity could serve as an alternative method to determine defect-induced phonon scattering mean free path that indirectly indicates the defect difference among samples.

With the knowledge of $l_0$ and $l_g$, the grain boundary thermal conductance in crystalline regions is analyzed. Just as mentioned previously, the thermal resistance arises from phonon to phonon scattering and phonon scattering by the grain boundary. Therefore, the thermal resistance relationship can be depicted as

$$l_g/k_{crystal} = R + l_g/k_g \quad (11)$$

Here $l_g$ is the grain size determined by XRD, and $k_g$ is the intrinsic thermal conductivity of the grain, respectively. $R$ is the grain boundary thermal resistance. Multiplying $\rho c_p$ on both sides of eq 11, $\Theta l_g = \Theta_i l_g + R\rho c_p$ can be determined. As temperature goes down to 0 K, $\Theta_i$ goes to zero; therefore, we can calculate the grain boundary thermal conductance as $G = R^{-1} = \rho c_p/(\Theta_0 l_g)$. $G$ could also be written as $G = \beta\rho c_p v$,[45] where $\beta$ is the grain boundary scattering coefficient and $\beta = l_0/l_g$. The grain boundary scattering coefficients are determined to be 0.409 and 0.478 for S1 and S2, respectively. Chen's work gives the grain boundary scattering coefficients for phonons diffuse scattering at the grain boundary for 3-D nonequilibrium thermal transport: $\beta = 3T_{d21}/\{4[1 - 0.5(T_{d12} + T_{d21})]\}$, where $T_{dij}$ is the energy transmissivity at an grain boundary for phonons incident from the $i$th layer toward the $j$th layer.[45] For the situation of diffuse scattering with $T_{d12} = T_{d21} = 0.5$, $\beta$ is 0.75 according to Chen's work. Compared with this characteristic scenario, our grain boundary scattering is a little weaker, but comparable. Then here if we assume $\beta$ is weakly frequency dependent, we can give a good estimation of the boundary thermal conductance using this equation $G = \beta\rho c_p v$. Figure 8b shows the temperature dependence of interface thermal conductance for S2. The high crystallinity and good crystallite orientation helps make the interface thermal conductance very high. At room temperature, the grain boundary thermal conductance is 3.73 GW/(m$^2$·K) for S2 ($R$, 0.268 × 10$^{-9}$ m$^2$·K/W). The thermal conductance decreases with the decreased temperature, and this trend is determined by $\rho c_p$ as shown in the equation $G = \beta\rho c_p v$. At 22 K, the thermal conductance becomes very small. The corresponding grain boundary thermal resistance is around 2.27 × 10$^{-9}$ m$^2$·K/W for S2. The order of grain boundary thermal resistance calculated for the UHMWPE crystal is comparable to interfacial thermal resistance of some other materials. Here, the interface thermal resistances of some other materials are presented to show the usual order of


DOI: 10.1021/acsami.5b08578
ACS Appl. Mater. Interfaces 2015, 7, 27279−27288

interface thermal resistance. For nanocomposites of PbTe/GeTe, the interface thermal resistance is around $0.73 \times 10^{-9}$ $m^2 \cdot K/W$ at 700 K.[46] Wei's work shows that the interface thermal resistance in multilayer graphene structures has an order of $10^{-9}$ $m^2 \cdot K/W$ at room temperature.[47] Even we give a 20% variation range for $\beta$; we get the same level of interface thermal conductance. The magnitude of $G$ remains the same, and the true thermal conductance should fall in this range well.

## 4. CONCLUSION

In this work, we characterized the thermal diffusivity and thermal conductivity of microscale UHMWPE fibers from room temperature down to 22 K and investigated the volumetric heat capacity, mean free path due to defects-induced phonon scattering, and grain boundary thermal conductance. Evaluation is also given for the thermal conductivity of pure crystalline PE fiber after taking out the amorphous effect. At room temperature, the thermal diffusivity and thermal conductivity of the samples were measured at around $1.376 \times 10^{-5}$ $m^2/s$ and 22.5 $W/(m \cdot K)$. The high crystallinity and excellent crystallite orientation (studied with XRD) make contributions to the high thermal conductivity. A newly defined parameter "thermal reffusivity" was introduced to explain the effect of defects in polymers. Because of defects-induced phonon scattering in the UHMWPE fibers, the thermal reffusivity was nonzero when temperature goes down to zero. The residual thermal reffusivities for the crystalline regions in two samples were determined as $3.45 \times 10^4$ and $2.95 \times 10^4$ $s/m^2$, respectively. The phonon mean free paths determined by defects in crystalline regions of S1 and S2 were calculated as 8.06 and 9.42 nm, respectively. These values were relatively smaller than the XRD-determined crystallite size of (002) plane in our samples: 19.7 nm. This strongly concluded that in the UHMWPE fibers we studied, the scattering by grain boundaries makes phonons lose most of their historical information, and the grain-boundary scattering is more kind of diffuse. We conclude that the grain boundary thermal conductance can be evaluated with a sound accuracy using this equation: $G \approx \beta \rho c_p v$. At room temperature, the grain boundary thermal conductance is 3.73 $GW/(m^2 \cdot K)$ for pure crystalline S2. The order of the interface thermal conductance increases from ~0.2 to ~ 4 $GW/m^2 \cdot K$ when temperature increases from 22 K to room temperature.

## AUTHOR INFORMATION

### Corresponding Author

*E-mail: xwang3@iastate.edu. Tel.: 01-515-294-8023. Fax: 01-515-294-3261.

### Notes

The authors declare no competing financial interest.

## ACKNOWLEDGMENTS

Support of this work by the Army Research Office (Grant W911NF-12-1-0272), the Office of Naval Research (Grant N000141210603), and the National Science Foundation (Grants CBET1235852 and CMMI1264399) is gratefully acknowledged. X.W. thanks the "Taishan Scholar" Program of Shandong Province, China, for partial support.

## REFERENCES

(1) Choy, C. L. Thermal-Conductivity of Polymers. *Polymer* **1977**, *18*, 984−1004.
(2) Laaber, D.; Bart, H. J. Chemical Resistance and Mechanical Stability of Polymer Film Heat Exchangers. *Chem. Ing. Tech.* **2015**, *87*, 306−311.
(3) Neikirk, C. C.; Chung, J. W.; Priestley, R. D. Modification of Mechanical Properties in Polymer Nanocomposites by the Incorporation of Specific Self-Complementary Hydrogen Bonding Interactions. *Polymer* **2015**, *79*, 212−220.
(4) Haynes, W. M. *CRC Handbook of Chemistry and Physics* (Internet Version), 96th ed.; CRC Press/Taylor and Francis Group: Boca Raton, FL, USA, 2015; Section 13, pp 3−4.
(5) Shen, S.; Henry, A.; Tong, J.; Zheng, R. T.; Chen, G. Polyethylene Nanofibres with Very High Thermal Conductivities. *Nat. Nanotechnol.* **2010**, *5*, 251−255.
(6) Givens, S. R.; Gardner, K. H.; Rabolt, J. F.; Chase, D. B. High-Temperature Electrospinning of Polyethylene Microfibers from Solution. *Macromolecules* **2007**, *40*, 608−610.
(7) Reneker, D. H.; Fong, H. Polymeric Nanofibers: Introduction. *ACS Symposium Series*; American Chemical Society: Washington, DC, USA, 2006; Vol. *918*, Chapter 1, pp 1−6, DOI: 10.1021/bk-2006-0918.ch001
(8) Rein, D. M.; Shavit-Hadar, L.; Khalfin, R. L.; Cohen, Y.; Shuster, K.; Zussman, E. Electrospinning of Ultrahigh-Molecular-Weight Polyethylene Nanofibers. *J. Polym. Sci., Part B: Polym. Phys.* **2007**, *45*, 766−773.
(9) Roncali, J. Conjugated Poly(Thiophenes): Synthesis, Functionalization, and Applications. *Chem. Rev.* **1992**, *92*, 711−738.
(10) Kume, S.; Yamada, I.; Watari, K.; Harada, I.; Mitsuishi, K. High-Thermal-Conductivity AIN Filler for Polymer/Ceramics Composites. *J. Am. Ceram. Soc.* **2009**, *92*, S153−S156.
(11) Wang, S. L.; Cheng, Y.; Wang, R. R.; Sun, J.; Gao, L. Highly Thermal Conductive Copper Nanowire Composites with Ultralow Loading: Toward Applications as Thermal Interface Materials. *ACS Appl. Mater. Interfaces* **2014**, *6*, 6481−6486.
(12) Shtein, M.; Nadiv, R.; Buzaglo, M.; Kahil, K.; Regev, O. Thermally Conductive Graphene-Polymer Composites: Size, Percolation, and Synergy Effects. *Chem. Mater.* **2015**, *27*, 2100−2106.
(13) Vasileiou, A. A.; Kontopoulou, M.; Docoslis, A. A Noncovalent Compatibilization Approach to Improve the Filler Dispersion and Properties of Polyethylene/Graphene Composites. *ACS Appl. Mater. Interfaces* **2014**, *6*, 1916−1925.
(14) Liu, Y. D.; Kumar, S. Polymer/Carbon Nanotube Nano Composite Fibers-A Review. *ACS Appl. Mater. Interfaces* **2014**, *6*, 6069−6087.
(15) Haggenmueller, R.; Guthy, C.; Lukes, J. R.; Fischer, J. E.; Winey, K. I. Single Wall Carbon Nanotube/Polyethylene Nanocomposites: Thermal and Electrical Conductivity. *Macromolecules* **2007**, *40*, 2417−2421.
(16) Choy, C. L.; Wong, Y. W.; Yang, G. W.; Kanamoto, T. Elastic Modulus and Thermal Conductivity of Ultradrawn Polyethylene. *J. Polym. Sci., Part B: Polym. Phys.* **1999**, *37*, 3359−3367.
(17) Choy, C. L.; Luk, W. H.; Chen, F. C. Thermal-Conductivity of Highly Oriented Polyethylene. *Polymer* **1978**, *19*, 155−162.
(18) Fujishiro, H.; Ikebe, M.; Kashima, T.; Yamanaka, A. Drawing Effect on Thermal Properties of High-Strength Polyethylene Fibers. *Jpn. J. Appl. Phys., Part 1* **1998**, *37*, 1994−1995.
(19) Scott, T. A.; de Bruin, J.; Giles, M. M.; Terry, C. Low-Temperature Thermal Properties of Nylon and Polyethylene. *J. Appl. Phys.* **1973**, *44*, 1212−1216.
(20) Zhao, J. H.; Jiang, J. W.; Wei, N.; Zhang, Y. C.; Rabczuk, T. Thermal Conductivity Dependence on Chain Length in Amorphous Polymers. *J. Appl. Phys.* **2013**, *113*, 184304.
(21) Hennig, J. Anisotropy and Structure in Uniaxially Stretched Amorphous High Polymers. *J. Polym. Sci., Part C: Polym. Symp.* **1967**, *16*, 2751−2761.
(22) Choy, C. L.; Chen, F. C.; Luk, W. H. Thermal-Conductivity of Oriented Crystalline Polymers. *J. Polym. Sci., Polym. Phys. Ed.* **1980**, *18*, 1187−1207.


DOI: 10.1021/acsami.5b08578
*ACS Appl. Mater. Interfaces* 2015, 7, 27279−27288

(23) Henry, A.; Chen, G. High Thermal Conductivity of Single Polyethylene Chains Using Molecular Dynamics Simulations. *Phys. Rev. Lett.* **2008**, *101*, 235502.
(24) Bunn, C. W. *Chemical Crystallography*; Oxford University Press: Amen House, London, 1945; Chapter 7, p 233.
(25) Guo, J.; Wang, X.; Wang, T. Thermal Characterization of Microscale Conductive and Nonconductive Wires Using Transient Electrothermal Technique. *J. Appl. Phys.* **2007**, *101*, 063537.
(26) Sato, H.; Shimoyama, M.; Kamiya, T.; Amari, T.; Sasic, S.; Ninomiya, T.; Siesler, H. W.; Ozaki, Y. Raman Spectra of High-Density, Low-Density, and Linear Low-Density Polyethylene Pellets and Prediction of Their Physical Properties by Multivariate Data Analysis. *J. Appl. Polym. Sci.* **2002**, *86*, 443−448.
(27) Riveiro, A.; Soto, R.; del Val, J.; Comesaña, R.; Boutinguiza, M.; Quintero, F.; Lusquiños, F.; Pou, J. Laser Surface Modification of Ultra-High-Molecular-Weight Polyethylene (UHMWPE) for Biomedical Applications. *Appl. Surf. Sci.* **2014**, *302*, 236−242.
(28) Feng, X.; Wang, X.; Chen, X.; Yue, Y. Thermo-Physical Properties of Thin Films Composed of Anatase TiO2 Nanofibers. *Acta Mater.* **2011**, *59*, 1934−1944.
(29) Lin, H.; Xu, S.; Wang, X. W.; Mei, N. Thermal and Electrical Conduction in Ultrathin Metallic Films: 7 nm down to Sub-Nanometer Thickness. *Small* **2013**, *9*, 2585−2594.
(30) Cheng, Z.; Xu, Z.; Xu, S.; Wang, X. Temperature Dependent Behavior of Thermal Conductivity of Sub-5nm Ir Film: Defect-Electron Scattering Quantified by Residual Thermal Resistivity. *J. Appl. Phys.* **2015**, *117*, 024307.
(31) Guo, J. Q.; Wang, X. W.; Zhang, L. J.; Wang, T. Transient Thermal Characterization of Micro/Submicroscale Polyacrylonitrile Wires. *Appl. Phys. A: Mater. Sci. Process.* **2007**, *89*, 153−156.
(32) Liu, G. Q.; Xu, S.; Cao, T. T.; Lin, H.; Tang, X. D.; Zhang, Y. Q.; Wang, X. W. Thermally Induced Increase in Energy Transport Capacity of Silkworm Silks. *Biopolymers* **2014**, *101*, 1029−1037.
(33) Chang, S. S. Heat-Capacities of Polyethylene from 2 to 360 K II. High-Density Linear Polyethylene Samples and Thermodynamic Properties of Crystalline Linear Polyethylene. *J. Res. Natl. Bur. Stand., Sect. A* **1974**, *78*, 387−400.
(34) Maxwell, J. C. *Electricity and Magnetism*, 3rd ed.; Clarendon: Oxford, U.K., 1904; Chapter 9, p 440.
(35) Mugishima, T.; Kogure, Y.; Hiki, Y.; Kawasaki, K.; Nakamura, H. Phonon Conduction in Polyethylene. *J. Phys. Soc. Jpn.* **1988**, *57*, 2069−2079.
(36) Kittel, C. *Introduction to Solid State Physics*. 5th ed.; John Wiley & Sons: New York, 1976; Chapter 6, p 171.
(37) Perepechko, I. *Low-Temperature Properties of Polymers*. 1st ed.; Pergamon Press Inc.: New York, 1980; Chapter 2, pp 67−69, DOI: 10.1016/B978-0-08-025301-5.50005-9.
(38) Xu, Z. L.; Wang, X. W.; Xie, H. Q. Promoted Electron Transport and Sustained Phonon Transport by DNA down to 10 K. *Polymer* **2014**, *55*, 6373−6380.
(39) Kittel, C. *Introduction to Solid State Physics*, 5th ed.; John Wiley & Sons: New York, 1976; Chapter 6, p 128.
(40) Cohen, A. F. Thermal Conductivity of Sodium Fluoride Crystal at Low Temperatures. *J. Appl. Phys.* **1958**, *29*, 870−870.
(41) Kirkham, A. J.; Yates, B. The Low-temperature Specific Heats and Related Thermodynamic Properties of Sodium Fluoride and Caesium Bromide. *J. Phys. C: Solid State Phys.* **1968**, *1*, 1162−1170.
(42) Stuart, S. J.; Tutein, A. B.; Harrison, J. A. A Reactive Potential for Hydrocarbons with Intermolecular Interactions. *J. Chem. Phys.* **2000**, *112*, 6472−6486.
(43) Genensky, S. M.; Newell, G. F. Vibration Spectrum and Heat Capacity of a Chain Polymer Crystal. *J. Chem. Phys.* **1957**, *26*, 486−497.
(44) Kolouch, R. J.; Brown, R. G. Thermal Conductivities of Polyethylene and Nylon from 1.2° to 20° K. *J. Appl. Phys.* **1968**, *39*, 3999−4003.
(45) Chen, G. Thermal Conductivity and Ballistic-Phonon Transport in the Cross-Plane Direction of Superlattices. *Phys. Rev. B: Condens. Matter Mater. Phys.* **1998**, *57*, 14958−14973.
(46) Huang, X. P.; Wang, X. W.; Cook, B. Coherent Nanointerfaces in Thermoelectric Materials. *J. Phys. Chem. C* **2010**, *114*, 21003−21012.
(47) Wei, Z. Y.; Ni, Z. H.; Bi, K. D.; Chen, M. H.; Chen, Y. F. Interfacial Thermal Resistance in Multilayer Graphene Structures. *Phys. Lett. A* **2011**, *375*, 1195−1199.


DOI: 10.1021/acsami.5b08578
*ACS Appl. Mater. Interfaces* 2015, 7, 27279−27288